Product Imaging Studies of Photodissociation and Bimolecular Reaction Dynamics

P. L. Houston,[1] B. R. Cosofret,[1] A. Dixit,[1] S. M. Dylewski,[2] J. D. Geiser,[1] J. A. Mueller,[1] R. J. Wilson,[1] P. J. Pisano,[1] M. S. Westley,[2] K. T. Lorenz,[3] and D. W. Chandler[3]

[1]Department of Chemistry and Chemical Biology
[2]Department of Applied and Engineering Physics
Cornell University
Ithaca, NY 14853-1301 USA
[3]Combustion Research Facility
Sandia National Laboratory
Livermore California USA

Abstract

This paper briefly reviews recent progress in product imaging studies of photodissociation and bimolecular reaction dynamics.

The $SO_2 + h\nu \rightarrow SO(^3\Sigma^-) + O(^3P_2)$ channel in the ultraviolet photodissociation of sulfur dioxide at photolysis wavelengths between 202 and 207 nm has been studied using resonance-enhanced multiphoton ionization with time-of-flight product imaging. These imaging experiments allowed the determination of the vibrational populations of the $SO(^3\Sigma^-)$ fragment at several wavelengths. A change in the vibrational populations occurs from a distribution where most of the population is in $v=0$ for wavelengths shorter than 203.0 nm to one where the population is more evenly distributed for longer wavelength dissociation. The changes in the internal energy distribution are attributed to participation of two different predissociation mechanisms. Our data suggest that the predissociation mechanism below 203.0 nm involves an avoided crossing with the repulsive singlet state $^1A_1$.

The $O_3(X\,^1A_1) + h\nu \rightarrow O(2p\,^3P_J) + O_2(X\,^3\Sigma_g^-)$ product channel in the UV photodissociation of ozone has been investigated at photolysis wavelengths of 226, 230, 233, 234, 240, and 266 nm. At 226, 230, 233, 234, and 240 nm, the yield of the O_2 product in vibrational states greater than or equal to 26 was 11.8±1.9%, 11.5±1.2%, 8.2±2.0, 4.7±1.8, and 0.6±0.1%, respectively.

Two-dimensional ion counting product imaging has also been used to determine the bond energy for the dissociation of jet-cooled O_3 into $O(^1D) + O_2(^1\Delta)$. The bond dissociation energy into $O(^1D) + O_2(^1\Delta)$ was found to be 386.59 ± 0.04 kJ/mol. The standard heat of formation of O_3 is calculated to be -144.31 ± 0.14 kJ/mol.

State-selective differential cross sections for rotationally inelastic scattering of NO (J_i = 0.5, 1.5, $F_1 \rightarrow J_f$ = 2.5–12.5, F_1 and J_f =1.5-9.5, F_2) from He and D_2 measured by crossed molecular beam ion imaging are reported. The images typically exhibit a single broad rotational rainbow maximum that shifts from the forward to the backward scattering direction with increasing ΔJ. The angle of the rainbow maximum was lower at a given ΔJ for D_2 than for He as a collision partner. At a collision energy of ~500 cm^{-1}, primarily the repulsive part of the potential surface is probed, which can be modeled with a 2-D hard ellipse potential. This model for rotationally inelastic scattering is shown to qualitatively match the experimental differential cross sections. A more advanced CEPA PES for NO+He does not give substantially better agreement with the experiment.

Introduction

Product imaging techniques have transformed the field of molecular dynamics, in part due to new techniques which greatly increase the resolution of the original technique.[1] In this method, the three-dimensional velocity distribution of products of a chemical reaction is projected onto a two-dimensional detector, and the resulting image is captured with a digital camera. The two-dimensional projection can be converted into the three-dimensional distribution by use of an inverse-Abel transformation.[2,3]

A problem in the resolution of the original technique is that there is a finite overlap volume between the molecular beam and the laser beams. This overlap causes a blurring of the resulting image. For example, if the overlap dimension is 1 mm, then the resolution of the image taken with a normal Wiley-McLaren time-of-flight mass spectrometer cannot be better than 1 mm. Fortunately, Eppink and Parker discovered that the use of an einzel lens can almost completely correct for this blurring.[4] Images collected using such a lens are called velocity mapped images.

Another improvement in the resolution is accomplished by an ion counting technique.[5] Ions hitting the screen are first discriminated from noise using a threshold function. On every shot of the laser, a computer program then locates the center of each cluster of ion pixels and replaces the cluster with a single count. The counts are then accumulated to produce an image.

Such improvements have made it possible to study a variety of new processes using product imaging. This paper will review some recent results from the laboratories of the authors.

Experimental

The experiments were performed either in an apparatus used primarily for photodissociation dynamics or in one used primarily for crossed beam molecular dynamics. The photodissociation apparatus has been described in detail elsewhere.[5,6,7] The parent compound was expanded typically in a 10% mixture with helium at a total pressure of 17 psi through a pulsed 250 µm diameter nozzle and collimated by a 500 µm diameter skimmer mounted about 1.0 cm from the nozzle orifice. Further downstream, the molecular beam was crossed at right angles by two counter-propagating laser beams, one used to dissociate the parent compound and the other to probe the resulting fragments. The ionized fragments were accelerated into a field-free flight tube mounted along the axis of the molecular beam. The ions were imaged by a position sensitive detector consisting of a chevron double micro-channel plate (MCP) assembly (Galileo) coupled to a fast phosphor screen. The image on the screen was recorded by a 640x480 pixel CCD camera (Xybion). Both the MCP and the camera were electronically gated to collect signal corresponding only to the mass of the probed fragment. Signal levels were kept below 300 ions per frame to assure accurate ion counting. Data were accumulated typically for 80,000 total laser shots.

The crossed molecular beam apparatus has also been described elsewhere.[8] Briefly, two molecular beams are generated in differentially pumped source chambers, pass through collimating apertures and intersect in an interaction chamber capable of maintaining a pressure of 7×10^{-7} torr with both molecular beams pulsed at 30 Hz. The products of the scattering reaction are state-selectively ionized in the interaction region by a focused, pulsed

probe laser. At the intersection region of the main chamber, a set of ion lenses mounted perpendicular to the plane of the molecular beams extract and focus the ions through a time-of-flight mass spectrometer (TOFMS) and onto a position sensitive MCP/Phosphor detector. The phosphor is imaged by a CCD camera and the signal is integrated over a succession of shots either on the CCD chip or in a computer. For the experiments described here, a 2% NO in Argon mixture was used for the NO molecular beam, while a neat expansion of D_2 or He was used for the scattering beam. The backing pressure behind each expansion was typically around 2 atm. The rotational distribution of NO in the molecular beam can be extracted from an ionization spectra of the NO and corresponds to a rotational temperature of about 2.5 K. This corresponds to 92% of the NO in J=0.5, 8% of NO in J=1.5 and less than 1% in J>1.5.

For the scattering measurements, NO ionization was effected by lightly focusing the output of a XeCl excimer pumped dye laser to obtain approximately 1 mJ/pulse of 225-227 nm light. The wavelength range corresponds to 1+1 REMPI through the A $^2\Sigma^+$ state of NO. P and R transitions were used to ionize the NO scattered into higher rotational states of the F_1 or F_2 spin multiplets by collisions with the scattering beam. For $F_1 \rightarrow F_1$ scattering, product molecules for J_f = 2.5 to 5.5 were detected by use of the P_{11} branch, J_f = 6.5 to 9.5 were detected using the R_{21} branch, and J_f > 9.5 where detected using the $R_{11}+Q_{21}$ branch. The Λ doublets probed by this choice of transitions for detection is as follows: P_{11}: $\Pi(A')$ or e; R_{21}: $\Pi(A'')$ or f; and $R_{11}+Q_{21}$: $\Pi(A')$ or e. For $F_1 \rightarrow F_2$ scattering, all of the transitions were probed using the R_{21} branch, which detects $\Pi(A')$ or e Λ doublets. The choice of a relatively high power probe laser, 1+1 (as opposed to 1+1') REMPI, and P and R transitions of NO were made to minimize the possible preferential ionization of NO due to any correlation of rotational alignment and laser polarization.

Results and Discussion

Photodissociation Dynamics of SO₂

Figures 1 and 2 show the Abel-transformed images of the $O(^3P_2)$ produced in the photodissociation of SO₂ at two different wavelengths, 202.12 and 205.35 nm, respectively. The polarization vector of the dissociation and ionization light was parallel to a vertical line in these images. Similar images were
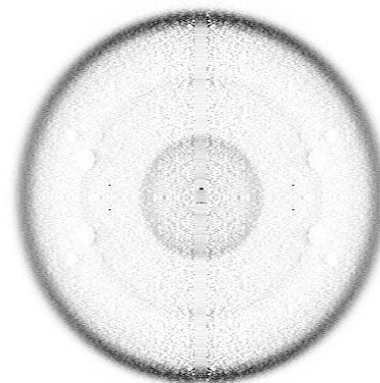
Figure 1 Abel-transformed image of the $O(^3P_2)$ product of SO₂ photodissociation at 202.13 nm.
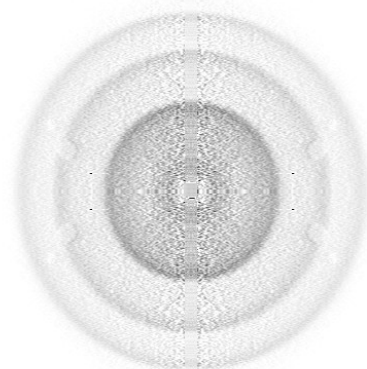
Figure 2 Abel-transformed image of the $O(^3P_2)$ product of SO₂ photodissociation at 205.35 nm.

obtained at a variety of wavelengths between 202 and 207 nm.[7] In each of these images, rings corresponding to the various vibrational levels of SO_2 can be observed and assigned according to the equation for conservation of energy:

$$KE = E_{hv} - D_0(\text{SO-O}) - E_{SO}(v, J), \quad \textbf{(1)}$$

where *KE* is the kinetic energy, $D_0(\text{SO-O})$ is the SO_2 dissociation energy, 5.65 ± 0.01 eV,[9] to form $SO(^3\Sigma^-) + O(^3P_2)$, and $E_{SO}(v,J)$ is the SO internal energy.

Table 1 shows the population in each vibrational mode of the SO fragment at six different photolysis wavelengths. The percentages are obtained by integrating the Abel transformed images over angle, plotting the result in energy space, fitting the peaks to Gaussians, and integrating the Gaussian for each vibrational level.

Table 1 Vibrational Distributions as a function of dissociation wavelength

Wavelength (nm)	% in $v = 0$	% in $v = 1$	% in $v = 2$	% in $v = 3$
202.13	73.7 ± 5.7	14.7 ± 1.4	7.9 ± 3.7	3.6 ± 1.0
202.80	51.9 ± 2.1	14.4 ± 0.6	17.8 ± 0.5	15.9 ± 1.2
202.90	43.8 ± 5.5	15.5 ± 2.0	20.6 ± 1.3	20.0 ± 2.1
203.00	33.7 ± 2.2	20.7 ± 0.6	27.3 ± 0.4	18.3 ± 2.0
205.35	28.7 ± 0.6	35.8 ± 1.2	35.5 ± 1.4	0
206.71	23.9 ± 1.2	37.9 ± 0.8	38.2 ± 0.6	0

The data of Table 1 show a striking change of the vibrational distribution near 203 nm. For example, note that the percent of population in $v = 0$ drops from 73.7% to 33.7% over less than a 1 nm change in dissociation wavelength. The vibrational populations measured in our experiments as a function of dissociation wavelength indicate that the internal energy distributions of the $SO(^3\Sigma^-)$ fragments do not depend on the vibrational modes excited, but instead are most sensitive to whether the dissociation is performed above or below the dissociation wavelength of 203.0 nm. This observation may indicate that the predissociation mechanism from the $\tilde{c}$ state changes at this wavelength, perhaps due to the avoided crossing between the excited $\tilde{c}(^1B_2)$ state of SO_2 and either of the repulsive $(3^1A')$ or corresponding triplet states.

Katagiri *et al.*[9] calculated crossing seams between the $\tilde{c}$ state and the repulsive singlet and triplet states by varying the R and γ coordinates when one S-O bond length is fixed at 2.706 a_0. The *ab initio* calculations showed that the bound $\tilde{c}\ ^1B_2$ ($2\ ^1A'$, in C_s geometry) and the repulsive singlet $(3^1A')$ states cross with each other almost diabatically. The two-dimensional potential energy surface calculated by Katagiri *et al*. shows the interaction between the $\tilde{c}$ state

and both the singlet and the triplet repulsive states; please refer to Fig. 9 of Ref. 9. The crossing seams between these states run along the energy contours on the outer wall of the bound potential energy surface of the $\tilde{c}$ state. Based on these observations, the authors concluded that the contribution from the dissociation through the mixing with the singlet and the triplet states may be quite small. They attributed the predissociation mechanism instead to an internal conversion in which the vibronic levels of the $\tilde{c}$ state couple with those of the ground electronic state, which correlates to the asymptote $SO(^3\Sigma^-) + O(^3P_2)$. However, since the dissociative wavefunctions on the repulsive states as well as the $\tilde{c}$ state vibrational wavefunction are seen theoretically to have large amplitudes along the crossing seams,[9] the dissociation via crossing with these repulsive states may have important contributions near the seam crossing energy regions.

The internal energy distribution results we have measured show that at dissociation wavelengths below 203 nm most of the internal energy of the $SO(^3\Sigma^-)$ fragment is in $v = 0$ (~75%), indicating very little internal energy excitation of the $SO(^3\Sigma^-)$ fragment. At dissociation wavelengths above 203 nm dissociation, we see a change in the energy distribution such that the internal energy of the SO fragment becomes more evenly distributed in $v = 0$,1, 2, and 3 (e.g. at 206.71 nm, ~24% in $v = 0$, ~34% in $v = 1$, and ~40% in $v = 2$). Without a change in dissociation mechanism, we would expect the vibrational distribution to evolve smoothly from low vibrational energy at high dissociation wavelengths to increased vibrational energy at shorter wavelengths. Not only does the observed distribution go in the opposite direction from this expectation, it changes abruptly at 203 nm. The abrupt change may indicate the onset of a second predissociation mechanism for the $\tilde{c}$ state of SO_2. The most likely explanation, then, for the vibrational distributions we find is that 203 nm corresponds to the energy of the seam between the excited $\tilde{c}$ state and one of these repulsive states, probably the singlet one.

The conclusion that a new predissociation channel opens at wavelengths below 203 nm is also consistent with the emission spectra excited near 200 nm in the work of Ray *et al.*,[10] which show strong emission into odd-v_3. Such a transition is nominally forbidden, but according to Ray *et al.* both the emission and absorption steps may become allowed if the A_1 electronic character of the intermediate repulsive state were to have strongly allowed transition via the a_1 component of the transition moment to the A_1 ground electronic state. They proposed that the intermediate state is the singlet repulsive state that undergoes curve crossing with the $\tilde{c}$ state.
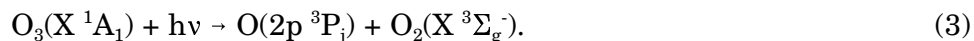
Photodissociation Dynamics of Ozone

The Triplet Channel

The Hartley band of ozone is a broad absorption feature from about 200 to 310 nm consisting of a continuum with some structure superimposed on it. Upon absorption, the molecule dissociates, predominantly following the spin-allowed channels

$$O_3(X\ ^1A_1) + h\nu \rightarrow O(2p\ ^1D_2) + O_2(a\ ^1\Delta_g) \tag{2}$$

and

$$O_3(X\ ^1A_1) + h\nu \rightarrow O(2p\ ^3P_j) + O_2(X\ ^3\Sigma_g^-). \tag{3}$$

The singlet channel is the dominant of these two channels with 85 to 90% of the molecules following this path. Interestingly, the minor triplet channel yields oxygen molecules with a bimodal energy distribution with a significant fraction of the molecules formed in very high vibrational states.[11] It is important to determine the quantity and fate of these energetic molecules generated in the stratosphere.

We have used resonance-enhanced multiphoton ionization coupled with time-of-flight product imaging to study the $O_3(X\ ^1A_1) + h\nu \rightarrow O(2p\ ^3P_j) + O_2(X\ ^3\Sigma_g^-)$ product channel in the UV photodissociation of ozone at photolysis wavelengths of 226, 230, 233, 234, 240, and 266 nm.[12] These imaging experiments, together with a measurement of the branching ratio into the different spin orbit states of the O atom, allowed the determination of the yields of the O_2 product in vibrational states greater than or equal to 26 as a function of wavelength.
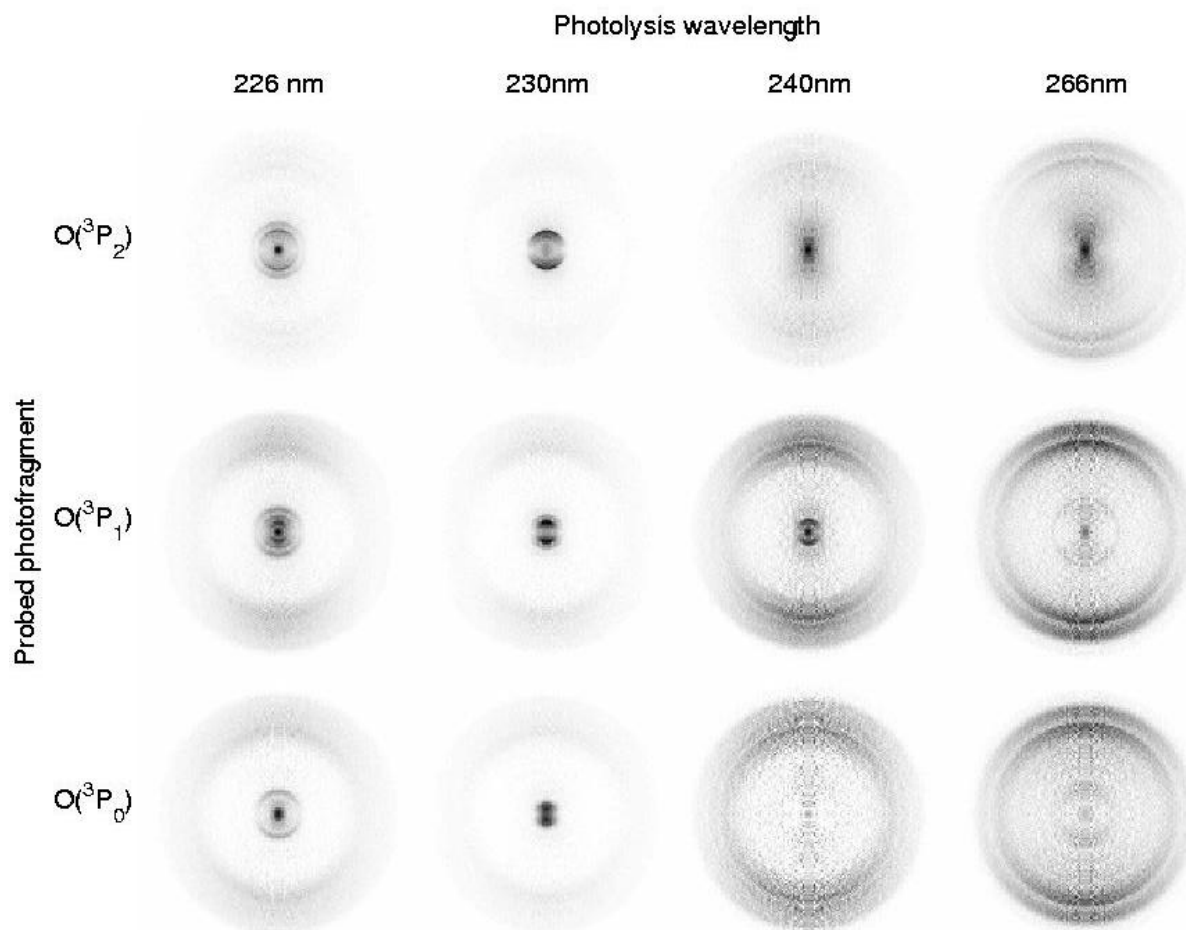
Figure 3 Table of the images of slices through the reconstructed 3D distributions of the O(^3P_j) fragments from ozone photodissociated at 226, 230, 240 and 266 nm.
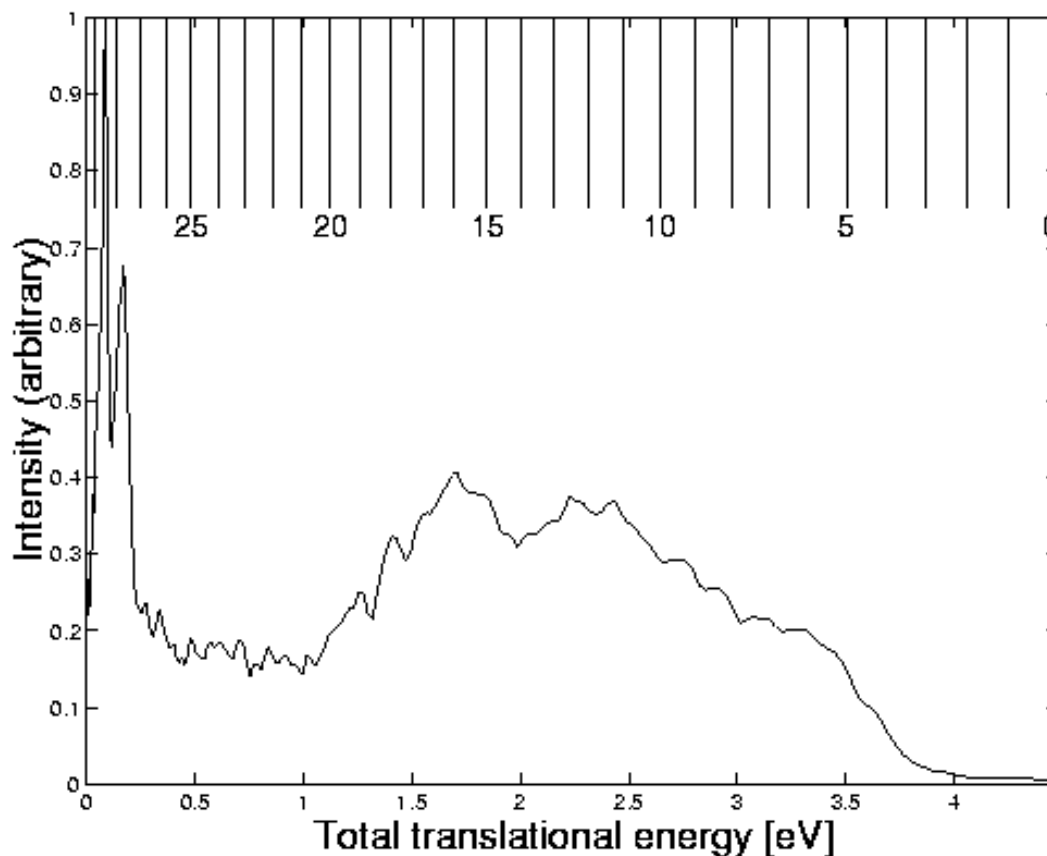
Figure 4 Total translational energy distribution of $O(^3P_2)$ and $O_2(^3\Sigma)$ products of photodissociation of ozone at 225.65 nm. The comb shows the corresponding vibrational levels of the $O_2(^3\Sigma)$.

Figure 3 displays slices through the reconstructed three dimensional distributions of the $O(^3P_j)$ fragments at four dissociation wavelengths. The electric vector of the dissociating and ionizing light is parallel to the vertical direction in the plane of the image. The recovered $O(^3P_j)$ velocity distributions from the inverse Abel transformed slices can be separated into angular and speed components. Angular distributions are determined by integrating over the desired speed interval for each angle. Extraction of the speed distribution is achieved in an analogous manner by integrating over all angles for each speed. The speed distributions can be further transformed, using the law of conservation of momentum, into total translational energy distributions for the $O_3 \rightarrow O_2(X\ ^3\Sigma_g^-) + O(^3P_j)$ dissociation. Figure 4 shows the total translational energy distribution of $O(^3P_2)$ for ozone dissociation at 226 nm.

The vibrational distribution of the O_2 product can then be determined by using conservation of energy,

$$KE = E_{h\nu} - D_0(O_2\text{-}O) - T_{O2}(v) + ZPE_{O2} - F_{v,O2}(J) - E_{O(3Pj)} \,, \tag{4}$$

where $D_0(O_2\text{-}O)$ is the ozone dissociation of energy 1.0523 ± 0.0026 eV, $T_{O2}(v)$ is the vibrational term, $F_{v,O2}(J)$ the rotational term calculated from spectroscopic constants, ZPE_{O2} is the zero point energy of the O_2 fragment, and $E_{O(3Pj)}$ are the $O(^3P_j)$ energies. Note from the comb of vibrational levels in Fig. 4 that the vibrational distribution of the $O_2(^3\Sigma)$ is bimodal, with one peak near $v = 27$ and another near $v = 15$.

It is interesting to note that virtually all of the oxygen molecules formed are vibrationally excited. The population of interest for the ozone deficit problem[11] is that in $v \geq 26$. This population is determined from the images for each spin-orbit state as a function of wavelength and are shown in Table 2.

Table 2 The percent population of O_2 from the triplet channel in $v \geq 26$ as a function of photolysis wavelength and spin-orbit state of the counter fragment. Note that the thermodynamic threshold for the generation of $O_2(v = 26)$ is at 241.6 nm.

	226 nm	230 nm	233 nm	234 nm	240 nm
$O(^3P_2)$	14.5 ± 2.0	16.8 ± 3.8	15.2 ± 0.2	6.9 ± 0.9	0.70 ± 0.10
$O(^3P_1)$	5.5 ± 0.5	5.1 ± 0.7	0.7 ± 0.2	0.8 ± 0.2	0.30 ± 0.10
$O(^3P_0)$	3.6 ± 0.5	4.1 ± 0.6	0.4 ± 0.2	0.6 ± 0.2	0.10 ± 0.05

Product imaging has thus provided detailed information on the vibrational distribution of $O_2(^3\Sigma_g^-)$ produced in the dissociation of ozone at wavelengths between 226 and 240 nm. The distributions for wavelengths of 233 nm and below are bimodal, with one peak in the distribution near $v=14$ and another near $v=27$. When combined with a measurement of the branching ratio to different spin-orbit states of the $O(^3P_j)$ atom,[12] it is possible to determine the fraction of $O_2(^3\Sigma_g^-)$ produced in levels $v \geq 26$ as a function of wavelength. At 226, 230, 233, 234, and 240 nm, the yield of the O_2 product in vibrational states greater than or equal to 26 was $11.8\pm1.9\%$, $11.5\pm1.2\%$, 8.2 ± 2.0, 4.7 ± 1.8, and $0.6\pm0.1\%$, respectively. The wavelength dependence of this fraction is similar to that used previously to calculate the effect of $O_2(^3\Sigma_g^-, v \geq 26)$ on the production rate of stratospheric ozone.[13] The bimodal vibrational distribution of the $O_2(^3\Sigma_g^-)$ suggests that there is more than one dissociation mechanism for production of $O_2(^3\Sigma_g^-)$. Additional hints about the dissociation mechanism are provided by the sharp onset with decreasing wavelength of the $O_2(^3\Sigma_g^-, v \geq 26)$ yield and by the variation in the vibrational distribution of $O_2(^3\Sigma_g^-)$ with the spin-orbit state of the sibling $O(^3P_j)$.

The Singlet Channel

The singlet channel of ozone photodissociation has also been examined using imaging techniques.[14] Figure 5 shows inverse Abel-transformed images of the $O(^1D)$ velocity at a variety of photodissociation wavelengths; they show clearly distinguished rings corresponding to the possible vibrational states of the sibling $O_2(^1\Delta_g)$. For example, in the fourth image in the top row (266 nm), there are four rings, corresponding to the only four vibrational levels

allowed by conservation of energy, $v = 0\text{-}3$. As the wavelength decreases, more rings become visible because more energy is available for vibrational excitation, whereas as the wavelength increases, the rings disappear one by one until only a single ring is evident at 300 nm.
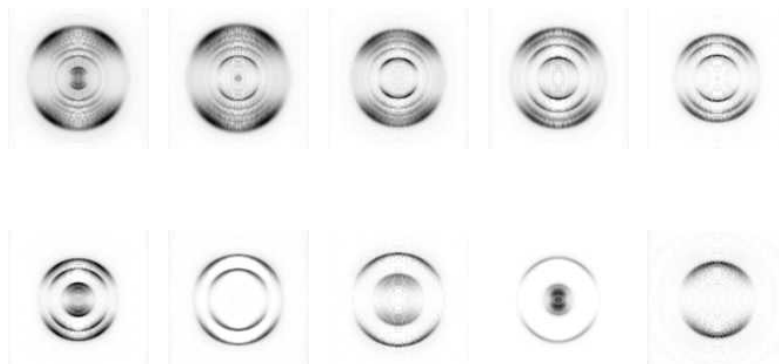
Figure 5 Inverse Abel-transformed images for O(^{1}D) from ozone photodissociation at 235, 245, 255, 266, 275, 279, 285, 290, 294, and 300 nm.

At 305.74 nm, the only vibrational level allowed is $v = 0$, and the rings observed in Fig. 6 correspond to *rotationally* allowed levels of the O$_2$($^1\Delta_g$). Assignment of these rotational levels has led to an improved dissociation energy for O$_3 \rightarrow$ O(^{1}D) + O$_2$($^1\Delta_g$) of 386.59 ± 0.04 kJ/mole.[15]
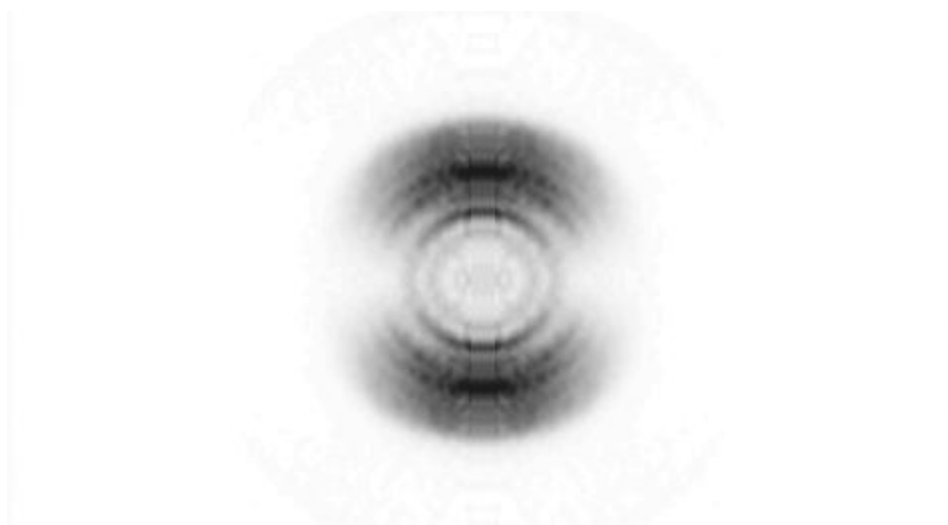
Figure 6 O(^{1}D) image following dissociation of ozone at 305.74 nm.

Inelastic Scattering of He and D_2 from NO

Rotationally inelastic scattering of molecules is of fundamental importance in energy transfer of molecular gases. Integral and differential cross sections for rotationally inelastic scattering of NO from collisions partners such as He, Ar, NO, and N_2 have been extensively studied. Along with these experimental studies, potential energy surfaces (PES) for NO-Ar and NO-He have been generated and tested against experimental results. The sheer volume of theoretical and experimental work done on NO is attributable to several factors. First, NO is experimentally convenient; it is one of the few radical species that is stable enough to be stored in a gas cylinder. Next, the spectroscopy of NO makes it very sensitive to laser based detection methods such as REMPI or LIF. Finally, NO is of theoretical interest, partially because of the extensive experimental work that has been done, but also because NO is a radical species with non-zero orbital angular momentum in its ground state, which gives rise to complex potential interactions.


Figure 7 Image for He-NO scattering into NO(J = 3.5)

Figure 8 Image for He-NO scattering into NO(J = 8.5)

The background subtracted ion images for He-NO and $J_i \sim 0.5$, $F_1 \rightarrow J_f = 3.5$ and 8.5, F_1 are shown in Figs. 7 and 8. Other images were taken for $J_f = 2.5 - 12.5$, F_1 as well as for $J_i \sim 0.5$, $F_1 \rightarrow J_f = 1.5 - 9.5$, F_2. Forward scattering intensity appears in the upper left portion of the scattering sphere, while backward scattering intensity appears in the lower right section of the scattering sphere. In order to orient the reader, a Newton diagram for the system is overlaid on the image for NO $(J_f = 5.5$, $F_1)$ in Figure 9. Qualitative interpretation of the images leads to the conclusion that there is a single broad peak that moves from forward to backward scattering with increasing ΔJ as previously observed for NO-He and NO-Ar inelastic scattering.[16,17,18,19]
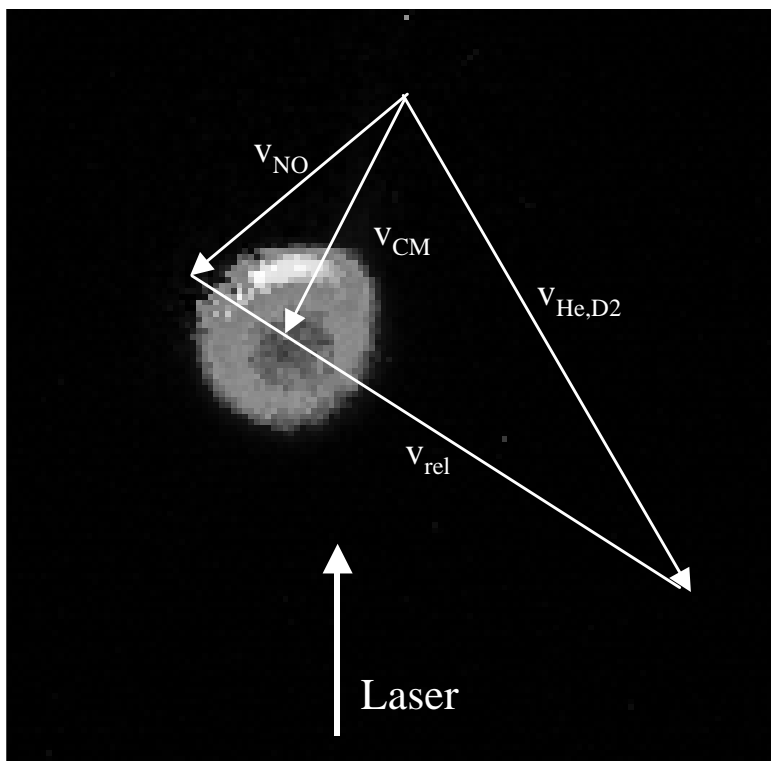
Figure 9 Typical image, with beam and center of mass velocities superimposed.

Similar results were found for the spin-orbit changing collisions (not shown) and for scattering of NO by D_2. Additionally, we observed that, for a given J, the position of the rainbow maximum is slightly more in the forward direction for D_2 than for He.

In order to interpret the data, two models have been used. The CEPA PES for NO+He of Yang and Alexander [20] has been used to generate theoretical differential cross sections, which are then compared to experiment. This PES is found to accurately reproduce the major features of the experimental data for NO+He with deviations in the positions of rainbow maxima. Due to the small differences between the differential cross sections for He and D_2, the NO+He PES also does a reasonable job predicting the angular distributions for scattering of NO+D_2, suggesting that this PES could be used to estimate NO+D_2 scattering measurements. Additionally, due to the seemingly simple behavior of the differential cross section as a function of ΔJ and scattering species, a two dimensional hard ellipse model was used to predict the scattering behavior for $F_1 \rightarrow F_1$ scattering. In general, by adjusting the anisotropy of the ellipse, the predicted rainbow maxima positions could be made to agree with the rainbow maxima from the data.

The most recent theoretical PES for NO+He scattering by Yang and Alexander has been used to produce theoretical differential cross sections using the numerical package entitled HIBRIDON™. HIBRIDON™ is a package of programs for the time-independent quantum treatment of inelastic collisions and photodissociation written by M. H. Alexander

et al.[21,22] The NO was assumed to have an initial population of 0.92 in J=0.5, F_1 and 0.08 in J=1.5, F_1 with an equal distribution between Λ doublet states. The Λ doublet state of the scattered NO was fixed by the transition used to ionize the NO. NO+He collisions were simulated at collision energies of 491 cm^{-1}. A comparison of the experimental differential cross sections with calculated cross sections from the Yang and Alexander (YA) PES and a hard ellipse model (details below) for selected spin-orbit conserving collisions is presented in Ref. 23, where the experimentally extracted NO/He DCSs are compared to the calculated YA DCSs and to DCSs extracted from images that have been simulated using the calculated YA DCSs as trial input cross sections. In general, the comparison shows that the procedure used for extraction of the DCSs is accurate.

The two dimensional hard ellipse model has been shown to accurately reproduce maxima in rotationally inelastic scattering angular distributions, known as rotational rainbows.[24,25] The basic premise of the model is that the potential energy surface for the interaction can be replaced by a two dimensional potential surface that has an infinitely high potential step on an elliptical contour. The shape of the ellipse can be estimated from the classical turning points of other potential surfaces. Such models predict, correctly, a rotational "rainbow" or peak in the angular distribution. The position of the maximum of this peak is determined solely by the collision energy and the relative sizes of the semimajor and semiminor ellipse axes A and B, respectively.

By adjustment of the ellipse parameters, especially the anisotropy (A-B), the rainbow maxima positions of the extracted DCSs for the rotational states for each of the NO+He and NO+D$_2$ collision systems can be fit to a relatively simple hard ellipse model. Figure 10 shows a comparison of rainbow maxima, θ_R, extracted from calculated DCSs using the YA PES, and those taken from the experimentally extracted DCSs, as well as a fit to the experimental NO+He rainbow positions. Data for J=9.5-10.5 have not been included in the fit because 1) the data do not conclusively show whether there is a peak in the angular distribution or whether the data is simply backscattered, and 2) there is an intrinsic uncertainty in the extraction procedure that makes the nearly backscattered peak positions very sensitive to the assumed position of the laser beam. For NO+He ($F_1 \rightarrow F_1$), the results of fitting the observed rainbow maxima positions to a 2-D hard ellipse model (solid line fit to closed circles) give results of (A-B) = 0.62Å and δ = 0.04Å (using A $\approx$ 2.7-3.1Å). The results for NO+D$_2$ ($F_1 \rightarrow F_1$) are found to be similar, but with noticeably higher anisotropy: (A-B) = 0.76Å and d = 0.14Å (using A $\approx$ 2.7-3.1Å). These model ellipse anisotropies can be compared to estimates of the anisotropy in the repulsive wall of the CEPA PES of Yang and Alexander. The YA PES contours near 500 cm^{-1} (comparable to the collision energy of our experiment) give values for A and B of ~2.8Å and ~2.4Å, respectively. This results in a value of (A-B) = 0.4Å, which is considerably less than the anisotropy given by the 2-D hard ellipse models extracted from either the NO/He or NO/D$_2$ data presented in this study. A lower repulsive anisotropy will result in scattering distributions that are positioned at higher deflection angles. This trend is shown in Figure 10. Note that the rainbow positions, derived from the YA DCSs are positioned to higher deflection angles relative to the 2-D hard ellipse rainbows for all J values. A small shift is expected because of the quantum nature of the HIBRIDON calculation,[26] but we don't believe that this explains the large shift we observe. In addition, the value of the YA theoretical θ_R rises more rapidly with J_f than the either of the hard ellipse models, to the point that there
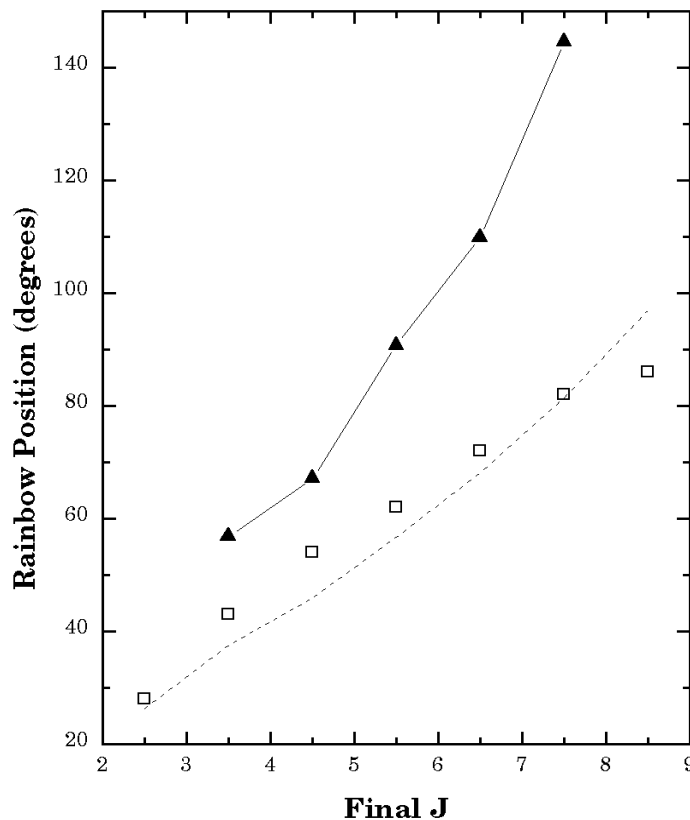
Figure 10 Plot of rainbow maxima versus J_f for data, the Yang-Alexander PES, and the hard ellipse models. Open squares are data for He/NO; the dashed lines is a fit to a hard-ellipse model for the He data; the triangles are HIBRIDON predictions for He/NO at a collision energies of 491 cm^{-1}.

may not be sufficient anisotropy for reaching the collisional energetic limit.

Conclusions

The product imaging technique has provided information on the internal energy of the SO($^3\Sigma^-$) fragment as a function of the dissociation wavelength.[7] A sudden change in the distribution at a dissociation wavelength of 203 nm suggests a change in the dissociation mechanism.

Product imaging has also provided detailed information on the vibrational distribution of O$_2$($^3\Sigma_g^-$) produced in the dissociation of ozone at wavelengths between 226 and 240 nm and

at 266 nm.[6] The distributions for wavelengths of 233 nm and below are bimodal, with one peak in the distribution near $v=14$ and another near $v=27$. At wavelengths of 244 nm or longer, the peak at the $v=27$ disappears. When combined with a measurement of the branching ratio to different spin-orbit states of the $O(^3P_j)$ atom, it is possible to determine the fraction of $O_2(^3\Sigma_g^-)$ produced in levels $v \geq 26$ as a function of wavelength. The wavelength dependence of this fraction is similar to that used previously to calculate the effect of $O_2(^3\Sigma_g^-, v \geq 26)$ on the production rate of ozone, so that we do not expect the conclusion to be different: production of $O_2(^3\Sigma_g^-, v \geq 26)$ may account for the ozone deficit near 40 km, but cannot account for the deficit at higher altitudes, even if all the $O_2(^3\Sigma_g^-, v \geq 26)$ leads to production of ozone via a reaction such as that with O_2 to form $O_3 + O$.[11] The vibrational distribution of the $O_2(^3\Sigma_g^-)$ and the angular distributions of individual parts of this distribution indicate that there is more than one dissociation mechanism for production of $O_2(^3\Sigma_g^-)$. Additional hints about the dissociation mechanism are provided by the sharp onset with decreasing wavelength of the $O_2(^3\Sigma_g^-, v \geq 26)$ yield and by the variation in the vibrational distribution of $O_2(^3\Sigma_g^-)$ with the spin-orbit state of the sibling $O(^3P_j)$.

The singlet channel of ozone dissociation, $O_3 + h\nu \rightarrow O(^1D) + O_2(^1\Delta)$, has also been elucidated by product imaging. Rotational analysis near the threshold for this process has provided more accurate thermochemical information.[15] The bond dissociation energy into $O(^1D) + O_2(^1\Delta)$ was found to be 386.59 ± 0.04 kJ/mol. The standard heat of formation of O_3 is calculated to be -144.31 ± 0.14 kJ/mol.

Differential cross sections for rotationally inelastic scattering of NO with He and D_2 at ~ 500 cm^{-1} collision energy have been measured using crossed molecular beam ion imaging and extracted using a new forward simulation basis image technique. The positions of the rainbow peaks obtained from the extracted differential cross sections for $J_f < 9.5$ are found to be well fit by a hard ellipse model. The differential cross sections obtained using the Yang and Alexander PES are typically more backward scattered than the data, indicating that the anisotropy of the repulsive wall of their potential may be too low. The data for $J_f > 9.5$ shows a larger change in the rainbow scattering angle than is predicted by extrapolation of the low-J hard ellipse model. The high-J_f peak positions are in closer agreement with the positions calculated by Yang and Alexander.

For spin-orbit conserving collisions, the NO scattered from D_2 is seen to be more forward scattered than the NO scattered from He. The differences in the differential cross sections between NO+He and NO+D_2 are small and are partially, but not totally, attributable to the higher collision energy of the NO+D_2 system. Only small differences are observed between the rainbow positions of the spin-orbit changing and spin-orbit conserving collisions.

Acknowledgments

References

1.   Chandler, D. W.; Houston, P. L. *J. Chem. Phys.* 1987, 87, 1445-1447.

2.   Castleman, K. R., *Digital Image Processing* (Prentice Hall, New Jersey, 1996).

3.   Heck, A. J. R, Chandler, D. W. *Ann. Rev. Phys. Chem.* 46, 335 (1995).

4.   Eppink, A. T. J. B.; Parker, D. H. *Rev. Sci. Instrum.* **1997**, *68*, 3477-3484.

5.   Chang, B.-Y.; Hoetzlein, R. C.; Mueller, J. A.; Geiser, J. D.; Houston, P. L. *Rev. Sci. Instrum.* **1998**, *69*, 1665-1670.

6.   Wilson, R. J.; Mueller, J. A.; Houston, P. L. *J. Phys. Chem. A* **1997**, *101*, 7593.

7.   Cosofret, B. R.; Dylewski, S. M.; Houston, P. L. "Changes in the vibrational population of SO($^3\Sigma^-$) from the photodissociation of SO$_2$ between 202 and 207 nm," *J. Phys. Chem.*, accepted for publication in the C. Bradley Moore Issue.

8.   Westley, M. S. Molecular Beam Studies of Inelastic and Reactive Scattering, Cornell University, 2000.

9.   Katagiri, H.; Sako, T.; Hishikawa, A.; Yazaki, T.; Onda, K.; Yamanouchi, K.; Yoshino, K. *J. Mol. Struct.* **1997**, *413-414*, 589-614.

10.   Ray, P. C.; Arendt, M. F.; Butler, L. J. *Journal of Chemical Physics* **1998**, *109*, 5221-30.

11.   Miller, R. L.; Suits, A. G.; Houston, P. L.; Toumi, R.; Mack, J. A.; Wodtke, A. M. *Science* **1994**, *265*, 1831-1838.

12.   J. D. Geiser, J. D.; Dylewski, S. M.; Mueller, J. A.; Wilson, R. J.; Houston, P. L.; Toumi, R. *J. Chem. Phys.* **2000,** *112***,** 1279-1286.

13.   Toumi, R.; Houston, P. L.; Wodtke, A. M. *J. Chem. Phys.* **1996**, *104*, 775-776.

14.   Geiser, J. D.; Dylewski, S. M.; Houston, P. L. "The Vibrational Distribution of O$_2$(a $^1\Delta_g$) produced in the Photodissociation of Ozone from 226-310 nm," in preparation.

15.   Taniguchi, N; Takahashi, K; Matsumi, Y.; Dylewski, S.; Geiser, J.; Houston, P. L. *J. Chem. Phys.* **1999** *111*, 6350-6355.

16.   Jons, S. D.; Shirley, J. E.; Vonk, M. T.; Giese, C. F.; Gentry, W. R. *Journal of Chemical Physics* **1996**, *105*, 5397- 407.

17.   Meyer, H. *Journal of Chemical Physics* **1995**, *102*, 3151- 68.

18.   Bontuyan, L. S.; Suits, A. G.; Houston, P. L.; Whitaker, B. J. *Journal of Physical Chemistry* **1993**, *97*, 6342- 50.

19.   Suits, A. G.; Bontuyan, L. S.; Houston, P. L.; Whitaker, B. J. *Journal of Chemical Physics* **1992**, *96*, 8618- 20.

20.   Yang, M.; Alexander, M. H. *J. Chem. Phys.* **1995**, *103*, 6973-83.

21.   Alexander, M. H.; Manolopoulos, D. E. *Journal of Chemical Physics* **1987**, *86*, 2044-50.

22.   Alexander, M. H.; Manolopoulos, D. E.; Werner, H. J.; Follmeg, B. HIBRIDON; 4.1 ed., 1996.

23.   Westley, M. S.; Lorenz, K. T.; Chandler D. W.; Houston, P. L. *J. Phys Chem.,* submitted.

24.   Bosanac, S.; Buck, U. *Chemical Physics Letters* **1981**, *81*, 315-19.

25.   Bosanac, S. *Physical Review A (General Physics)* **1982**, *26*, 816-24.

26.   R. Schinke, *J. Phys. Chem.* **1986**, *90*, 1742-1751.